Reversible Stream Drop Transition in a Microfluidic Coflow System via On Demand Exposure to Acoustic Standing Waves

E. Hemachandran,[1,*] S. Z. Hoque,[1,*] T. Laurell,[2] and A. K. Sen[1,*,†]
[1]*Fluid Systems Lab, Department of Mechanical Engineering, Indian Institute of Technology Madras, 600036 Chennai, India*
[2]*Division of Nanobiotechnology, Department of Biomedical Engineering, Lund University, 22363 Lund, Sweden*

(Received 13 January 2021; revised 16 July 2021; accepted 18 August 2021; published 20 September 2021)

Transition between stream and droplet regimes in a coflow is typically achieved by adjusting the capillary numbers (Ca) of the phases. Remarkably, we experimentally evidence a reversible transition between the two regimes by controlling exposure of the system to acoustic standing waves, with Ca fixed. By satisfying the ratio of acoustic radiation force to the interfacial tension force, $\mathrm{Ca}_{\mathrm{ac}} > 1$, experiments reveal a reversible stream drop transition for $\mathrm{Ca} < 1$, and stream relocation for $\mathrm{Ca} \geq 1$. We explain the phenomenon in terms of the pinching, advection, and relocation timescales and a transition between convective and absolute instability from a linear stability analysis [P. Guillot *et al.*, Phys. Rev. Lett. **99**, 104502 (2007)].

DOI: 10.1103/PhysRevLett.127.134501

A continuous stream of a fluid in contact with another immiscible fluid can break into drops hallmarked by the Rayleigh-Plateau instability [1,2]. The instability is a direct consequence of the minimization of interfacial energy, related to interfacial tension and hydrodynamic force [3]. In a confined system such as a microchannel, drops are typically produced using a flow-focusing or T junction [4–6]. Drop formation can occur either at the junction, as observed in squeezing and dripping regimes, or downstream at the end of a liquid jet, as in the jetting regime [7–9]. While the dripping regime is a consequence of absolute instability, droplets in the jetting regime are produced through convective instability [10,11]. At higher Ca of the streams, growth of instability is suppressed as it gets entirely convected downstream resulting in the parallel flow regime and droplets are not formed [9,12]. The transition from the stream to the droplet regime and vice versa is typically achieved by adjusting the flow rate, consequently modifying the Ca of the phases [4]. However, the transition between the regimes achieved by altering the Ca inherits a longer time delay due to the response time of the fluidic system [13,14]. One means of generating drops while operating at a higher and fixed Ca, and achieving fast reversible transition between stream and droplet regimes would be to trigger the system with an external perturbation. Acoustic radiation force (ARF) due to standing bulk acoustic waves (BAW) can relocate coflowing immiscible streams [15,16] and introduce perturbation [14]. The transition between stream and drop regimes by controlling the acoustic field will be advantageous as it does not require changing the Ca and therefore can offer a fast response time. This would be of significant scientific interest, and also of great value for technologies that require on-demand and fast transition between the stream and drop regimes, such as microfluidics [17,18], emulsification [19], and encapsulation [20,21]. Despite great technological potential and scientific as well as industrial interest in droplet microfluidics, on-demand controlled generation of droplets at high Ca and reversible transition between the stream and drop regimes without altering the Ca have never been demonstrated.

In this Letter, we report for the first time the observation of a reversible transition between stream and droplet regimes by exposing a coflow of immiscible liquids to a

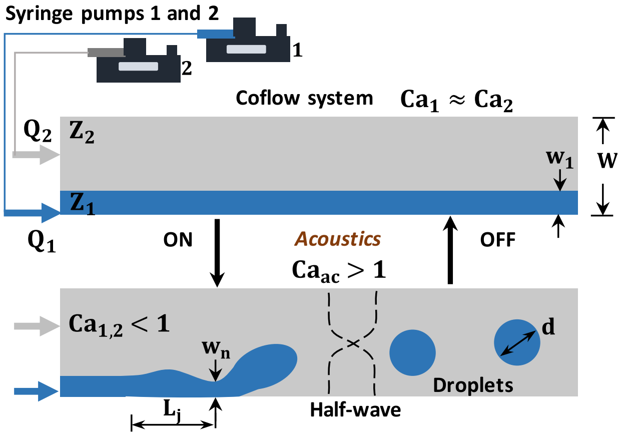

FIG. 1. Schematic of acoustic-driven on-demand and reversible stream–droplet (SD) transition: the establishment of a coflow system between stream 1 and 2 requires capillary numbers of both streams to be nearly the same $\mathrm{Ca}_1 \approx \mathrm{Ca}_2$, for $\mathrm{Ca}_{1,2} < 1$, with acoustic impedance $Z_1 > Z_2$, by switching on the acoustic field, satisfying acoustocapillary number $\mathrm{Ca}_{\mathrm{ac}} > 1$, stream to drop transition is observed, the reversal of drop to stream occurs by switching off the acoustic field. Length of the jet is L_j, width of the neck is w_n and droplet diameter is d.

standing BAW, without altering the Ca of the two phases (Fig. 1). Here, $\mathrm{Ca}_i = (\mu_i U_i/\gamma_{12})$, $i = 1, 2$ respectively, for streams 1 and 2, μ_i is the dynamic viscosity and U_i is the average velocity of the corresponding phase, and γ_{12} is the interfacial tension between the phases. We use a microchannel device with a coflow system and identify the conditions for reversible transitions in terms of the Ca and acoustocapillary number $\mathrm{Ca}_{\mathrm{ac}} = (E_{\mathrm{ac}}\overline{\Delta Z}W/\gamma_{12})$, where E_{ac} is the acoustic energy density [22], $\overline{\Delta Z} = (Z_1 - Z_2)/Z_{\mathrm{avg}}$ is the normalized acoustic impedance contrast, $Z_{\mathrm{avg}} = (Z_1 + Z_2)/2$, Z_1 and Z_2 are, respectively, acoustic impedances of streams 1 and 2, and W is the channel width [16,20]. We characterize stream drop transition and stream relocation in terms of the Ca of the phases. We study the growth and suppression of instability upon switching ON and OFF the acoustic field, respectively in terms of the variation of the width of the stream at the necking region and jet length with time. We explain the regimes in terms of the relevant timescales and a transition between convective and absolute instability.

The experiments are performed using a silicon-glass microfluidic device comprising two inlet channels of 250 μm width leading through a Y junction to an expanded channel of 370 μm width, with channel depth 100 μm throughout (see S1 in Supplemental Material [23]). The angle of the Y junction is kept large (>110°) to avoid localized radiation force and streaming effects [24,25]. As silicon and glass are hydrophilic, to facilitate the production of aqueous droplets, channels are chemically treated [26]. A pair of immiscible fluids are infused through the inlets with a syringe pump to establish a stable coflow. The different combinations of fluids used and their properties are presented in Tables S1 and S2 in Supplemental Material [23], which includes Refs. [27–29]. Surfactants [30,31] are used to control interfacial tension (IFT) between the phases, measured using the pendant drop method. In a given pair, the stream of higher acoustic impedance is taken as the inner phase, i.e., stream 1, and that of lower acoustic impedance forms the outer phase, i.e., stream 2. Standing BAW is produced in the expanded channel by actuating a PZT transducer bonded [32] to the bottom of the device at 0–28 Vp-p and frequency range 1.9–2.3 MHZ, depending on the fluid combination [33], using an amplified rf signal from a function generator. By maintaining the half-wavelength equal to the channel width, a standing wave is formed with its node at the center of the channel and antinodes at the side walls. For each pair of fluid, the acoustic energy density is obtained experimentally (see S2 in Supplemental Material, which includes Refs. [34,35]). The system is imaged with a high-speed camera through a microscope.

A stable coflow with a flat interface is established by maintaining, $\mathrm{Ca}_1 \approx \mathrm{Ca}_2$, with $\mathrm{Ca}_{1,2} \geq 0.01$, as indicated by the "coflow regime" in Fig. S1 (see S3 in Supplemental Material, which includes Ref. [36]). For $\mathrm{Ca}_{1,2} < 0.01$ and $\mathrm{Ca}_1 \neq \mathrm{Ca}_2$, owing to hydrodynamic instability, stream 1 forms a jet from which liquid droplets or plugs are produced [4] (see S2 in Supplemental Material [23]). The critical Ca in the present case is one order of magnitude smaller compared to the transition $\mathrm{Ca} \approx 0.1$ between threading and jetting regimes in a flow-focusing device [4], which can be attributed to the vicinity of the stream 1 to channel wall that tends to dampen perturbations [37]. The width of stream 1 depends on flow rate ratios as $w_1 \sim (Q_1/Q_2)^{0.5}$ (see Fig. S3). When such a coflow system is exposed to standing BAW, the dynamics will depend on acoustic impedance contrast between the streams, $\Delta Z = (Z_1 - Z_2)$ [16]. If $\Delta Z = 0$, or, $\Delta Z \neq 0$ and acoustocapillary number, $\mathrm{Ca}_{\mathrm{ac}} < 1$, the native flow configuration will be maintained. However, if $\Delta Z \neq 0$ and $\mathrm{Ca}_{\mathrm{ac}} > 1$, stream 1, having a higher acoustic impedance will relocate to the nodal plane at the center of the channel, owing to the ARF acting at the interface between the liquids. When we exposed a coflow system of aqueous glycerol (80%) and mineral oil with $\Delta Z > 0$ and $\mathrm{Ca}_{\mathrm{ac}} > 1$, for $\mathrm{Ca} < 1$, strikingly, we observed the aqueous stream breaks into a continuous stream of droplets [Fig. 2(a) and Supplemental Material [23], Movie 1]. The droplets migrate to the channel center owing to the ARF [20]. Upon switching off the acoustic field, the streams return to their native coflow configuration. So, we observed reversible stream drop (SD) transition simply by tuning the acoustic field ON and OFF without altering the original flow condition, or the Ca. On the other hand, for $\mathrm{Ca} > 1$, stream 1 does not break and instead relocates to the channel center as a liquid thread [see Fig. 2(b) and Supplemental Material [23], Movie 2]. The streams regain their native configuration when the acoustic field is turned off, depicting reversible stream thread (ST) transition. Similar results were obtained with other fluid combinations satisfying the above conditions.

When the coflow system shown in Fig. 2(a) is exposed to standing waves, with $\Delta Z > 0$, $\mathrm{Ca}_{\mathrm{ac}} > 1$, and $\mathrm{Ca} < 0.5$, we observe perturbations along the interface, as shown in Fig. 3(a)(i). There is a spatiotemporal variation in the width

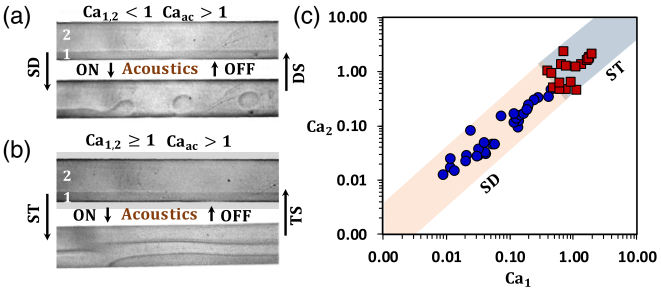

FIG. 2. Experimental images showing reversible (a) stream drop (SD) transition, for $\mathrm{Ca}_{1,2} < 1$ and $\mathrm{Ca}_{\mathrm{ac}} > 1$, Movie 1, (b) stream thread (ST) trasition, for $\mathrm{Ca}_{1,2} > 1$ and $\mathrm{Ca}_{\mathrm{ac}} > 1$, Movie 2. Stream 1: Aqueous glycerol (80%), Stream 2: mineral oil. (c) SD and ST regimes for the different combinations of fluids as streams 1 and 2 presented in Supplemental Material, Table S1 [23].

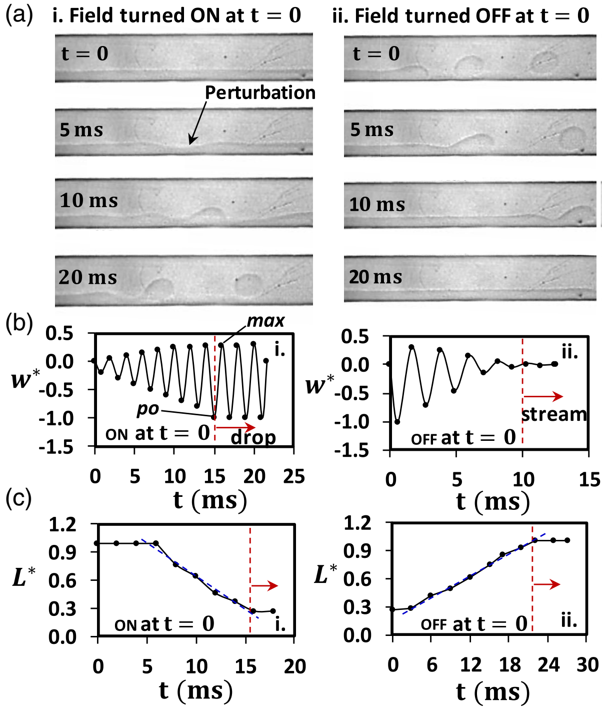

FIG. 3. (a) Experimental images showing the growth and suppression of instability upon switching (i) ON and (ii) OFF the acoustic field, respectively. (b) Variation of the dimensionless width of the stream, $w^* = (w_n - w_1)/w_1$, at the necking region with time, when the acoustic field is turned (i) ON and (ii) OFF. (c) Variation of dimensionless jet length, $L^* = (L_j/W)$, with time, when the acoustic field is switched (i) ON and (ii) OFF. Stream 1: Aqueous glycerol (80%) at flow rate 5 μL/ min, Stream 2: mineral oil at flow rate 35 μL/ min, applied voltage 16.1 V$_{pp}$, and frequency 2.1 MHz.

of streams, with amplitude growing with time, eventually resulting in pinching of the stream [Fig. 3(b)(i)]. The stream breaks into droplets leaving a jet whose length decreases with time until a spatially steady jet of a fixed length is established [Fig. 3(c)(i)]. The length of the steady jet is found to be proportional to Ca of the streams, $L_j \propto$ Ca, in agreement with literature [14]. The transition from stream to droplet regime is attributed to propagation of instability upstream, referred to as absolute instability [10]. The spatial undulations at the tip of the jet leads to pulsing of liquid in the form of a liquid bulb toward the center of the channel and then to droplet pinch-off (see Supplemental Material, Movie 1 [23]). The jet exhibits an oscillation pattern similar to capillary wave-induced oscillation due to surface tension gradient [38] that controls its thickness at its neck [Fig. 3(b)(i)]. Immediately after pinch-off, marked by “po,” the thickness of the neck increases linearly with time, exceeds the native stream width, and attains a maximum value, marked by “max.” Then it decreases linearly with time, falls below the original stream width, and finally goes to zero just when pinch-off occurs. When the acoustic field is turned off, an opposite scenario is observed [see Fig. 3(a)(ii)]: amplitude of neck thickness decreases with time [Fig. 3(b)(ii)], and jet length increases with time [Fig. 3(c)(ii)]. The neck travels downstream at a speed equal to that of the stream indicating that instability is convected downstream, returning to the stream regime. The transition from droplet to stream regime is attributed to the transition from absolute to convective instability wherein instability is carried downstream by the flow and does not perturb the system. When the coflow system in Fig. 2(b) is exposed to sound waves, with $\Delta Z > 0$, $\mathrm{Ca}_{\mathrm{ac}} > 1$, and $\mathrm{Ca} > 1$, we observe the high impedance stream relocates to the channel center as a liquid thread and is surrounded by the continuous phase. Although the interface between the streams appears to be undulated owing to the instability arising from the ARF, the coflow configuration is maintained indicating the existence of convective instability [see Fig. 2(b) and Supplemental Material [23], Movie 2]. Upon switching off the acoustic field, the streams regain their initial coflow configurations with both streams flowing closer to the side walls.

First, we evaluated the possible role of acoustic streaming on the instability and found that streaming has a negligible effect on the stream breakup and relocation phenomenon (see S12 in Supplemental Material [23]). The acoustic radiation pressure (ARP) acting on the fluids is of the order $f_p \approx \Delta\langle p_2^L\rangle \sim 10$ Pa, where $\Delta\langle p_2^L\rangle$ represents the mean Lagrangian pressure difference across the interface (see S10 in Supplemental Material [23], which includes Refs. [39–43]). The streaming induced shear stress (SIS) is scaled as $\eta\nabla v_R \approx \eta v_R/\delta$, where v_R is the streaming velocity and δ is the size of the streaming vortex, which is defined as the orthogonal distance from the boundary to the center of the vortex [25]. From simulations (see Supplemental Material S11 for the numerical model, which includes Refs. [44–49] and S12 for acoustic streaming effect, which includes Refs. [17,43,47,50]), we get $v_R \sim 10^{-5}$ m/s and $\delta \sim 10$ μm. So the ratio of the ARP to SIS scales as $\sim 10^3$, suggesting we can safely neglect the SIS. Further, our simulation results (see Supplemental Material S13 for numerical model, which includes Refs. [51–53], and S14 for simulation results) for the stream breakup by considering ARP and neglecting streaming effects reinstate that here the droplet breakup phenomenon is indeed driven by the ARP force. Here, $\mathrm{Bo} \ll 1$ and Reynolds number $\mathrm{Re} \ll 1$, so the gravitational and inertial forces are also negligible. So we note that ARF that tends to relocate the streams, deforms the interface and triggers the initial perturbation, and the interfacial dynamics is governed by the interplay of ARF, IFT, and viscous forces. We note that Kelvin-Helmholtz (KH) instability and pressure pulse-induced instability are suppressed (see S8 in Supplemental Material, which includes Refs. [54–58]). IFT amplifies the initial perturbation which can then lead to the destabilization of the interface attributed to the Rayleigh-Plateau instability [9,10].

We explain the coflow and droplet regimes in terms of the (i) pinch-off timescale $\tau_{\mathrm{po}} \sim (\mu_1 w_1/\gamma_1)$ which represents how fast the interface is pinched, (ii) advection timescale $\tau_{\mathrm{ad}} \sim (W/U_{\mathrm{av}})$, where U_{av} is the average velocity of the phases, and (iii) acoustic relocation timescale, $\tau_{\mathrm{re}} = (\mu W/E_{\mathrm{ac}} l \hat{\rho})$, where μ is the average viscosity, $\hat{\rho}$ is the normalized density contrast, and $l \approx 0.02$ times the channel width (W) [59]. The ratio of the pinch-off and advection timescales gives $\mathrm{Ca} = (\tau_{\mathrm{po}}/\tau_{\mathrm{ad}})$. We find all cases that exhibit droplet regime, $\tau_{\mathrm{po}} \sim 10$–$100$ ms and $\tau_{\mathrm{ad}} \sim 100$–$1000$ ms, which gives $\mathrm{Ca} < 1$. Since $\tau_{\mathrm{po}} < \tau_{\mathrm{ad}}$; stream 1 gets pinched completely. Herein, IFT amplifies the perturbation to minimize surface energy and viscosity fails to dissipate the same, and flow is not adequately fast for the disturbance to get convected downstream. Collectively these effects result in the rapid growth of instability leading to stream breakup and droplet production. Here, $\tau_{\mathrm{re}} \sim 100$ ms, and $\tau_{\mathrm{po}} < \tau_{\mathrm{re}} < \tau_{\mathrm{ad}}$, so before the stream relocates to the channel center, pinch-off takes place at a short distance from the channel inlet producing droplets [Fig. 2(a)]. Further, the acoustic migration timescale, $\tau_{\mathrm{ac}} \sim (\mu_2 W/d^2 E_{\mathrm{ac}} \Phi k) \sim 10$ ms $< \tau_{\mathrm{ad}}$, so droplets migrate to the nodal plane within a short distance after pinch-off region. In contrast, in all cases exhibiting stream relocation, $\tau_{\mathrm{po}} \sim 100$–$1000$ ms and $\tau_{\mathrm{ad}} \sim 100$ ms, which gives $\mathrm{Ca} > 1$. Here, $\tau_{\mathrm{re}} < 100$ ms and $\tau_{\mathrm{po}} > \tau_{\mathrm{ad}} > \tau_{\mathrm{re}}$, so instability is either suppressed by viscosity and/or convected downstream due to a faster flow thereby preventing stream breakup, and the stream relocates to the nodal plane within a short distance from the channel inlet [Fig. 2(b)]. In the limit of $\mathrm{Ca}_{\mathrm{ac}} \ll 1$, we find that $\tau_{\mathrm{re}} \gg \tau_{\mathrm{po}}$, τ_{ad} and stream remains unperturbed for $\mathrm{Ca} > 0.01$. For $\mathrm{Ca} < 0.01$, $\tau_{\mathrm{po}} \ll \tau_{\mathrm{ad}}$ and breakup occurs even without the acoustic perturbation (see Fig. S2 in Supplemental Material [23]).

Next, we verify the interpretation of our experimental results from a linear stability analysis [60,61]. Stream 1, which tends to relocate to the channel center, is surrounded by stream 2 and therefore we can approximate the flow configuration to be coaxial, wherein the stability is governed by the sign of the velocities ($\tilde{v}^*_\mp$) given as [60,61] $\tilde{v}^*_\mp = \{[\mathrm{Ca}\beta^3 G(\beta,\xi) \mp \kappa F(\beta,\xi)]/[\beta^9(1-\xi^{-1})-\xi^5]\}$. Here, $\beta = (w_1/w_2)$, w_1 and w_2 are the width of stream 1 and stream 2, respectively, $\xi = (\mu_1/\mu_2)$, μ_1, and μ_2 are the viscosities of the stream 1 and stream 2, respectively, $\kappa \approx 1.622$ is a constant [60,61], $G(\beta,\xi) = -4\beta + (8-4\xi^{-1})\beta^3 + 4(\xi^{-1}-1)\beta^5$, and $F(\beta,\xi) = \beta^4[4-\xi^{-1}+4\ln(\beta)] + \beta^6(-8+4\xi^{-1}) + \beta^8[4-3\xi^{-1}-(4-4\xi^{-1})\ln(\beta)]$. The above expression is obtained from the resulting dispersion equation by considering the spatiotemporal variation of perturbations varying as $e^{(ikx+\omega t)}$, with $k = (k_r + ik_i)$, and $\omega = (\omega_r + i\omega_i)$. The velocities $\tilde{v}^*_+$ and $\tilde{v}^*_-$ correspond to the maximal growth rate ω_r and extremal velocity of the envelope of the perturbation, $v = (\omega_r/k_i)$. The sign of $\tilde{v}^*_+$ indicates whether the stream is stable or unstable. If $\tilde{v}^*_+ < 0$ the stream is linearly stable, and for $\tilde{v}^*_+ > 0$, perturbation grows leading to instability. The sign of $\tilde{v}^*_-$ governs the nature of the instability: if $\tilde{v}^*_- < 0$, disturbances also travel upstream and the stream becomes absolutely unstable, and if $\tilde{v}^*_- > 0$, instability is convective as disturbances are convected downstream, and $\tilde{v}^*_-(\mathrm{Ca},\beta,\xi) = 0$ represents a transition between the two regimes. Herein, for all values of Ca, β, and ξ, $\tilde{v}^*_+ > 0$, so perturbation grows leading to instability. We find that for $\mathrm{Ca} < 1$, wherein stream droplet (SD) transition occurs, $\tilde{v}^*_- < 0$, indicating absolute instability. On the other hand, $\tilde{v}^*_- < 0$ for $\mathrm{Ca} > 1$, which indicates that the instability is convected downstream preventing stream break up and resulting in stream relocation (SR). The experimental data obtained for the different ξ, β, and Ca are presented on a (β,ξ) plane with respect to the $\tilde{v}^*_-(\mathrm{Ca},\beta,\xi) = 0$ lines for $\mathrm{Ca} = 1.0$ (Fig. 4). Strikingly, we observe that the large set of data collapses well corresponding to the SD transition and SR regimes, as can be seen by the grouping of the symbols.

In stream drop transition, while breaking of initial stream results in nonuniform drops, once a spatially steady jet is established, uniform drops are produced (see Supplemental Material, Fig. S5 and Movie 1 [23]). The droplets are in the size range 100–200 μm, and produced at ~500 drops per second. Since coflow condition requires $\mathrm{Ca}_1 \approx \mathrm{Ca}_2$ and, the size of the drops (d) is proportional to the stream width (w_1), by equating the Ca of the streams just upstream of the breakup region, and approximating the droplet diameter as the stream width and width of the continuous phase is very close to the channel width, we get $(d/W) \sim (\mu_1/\mu_2)^{1/2}(Q_1/Q_2)^{1/2}$. This simple scaling for droplet diameter is in remarkable agreement with experimental data (see Fig. S4). From experiments, we find that drop diameter depends on the ratio of flow rates and viscosities of streams, and is independent of the acoustic energy, given

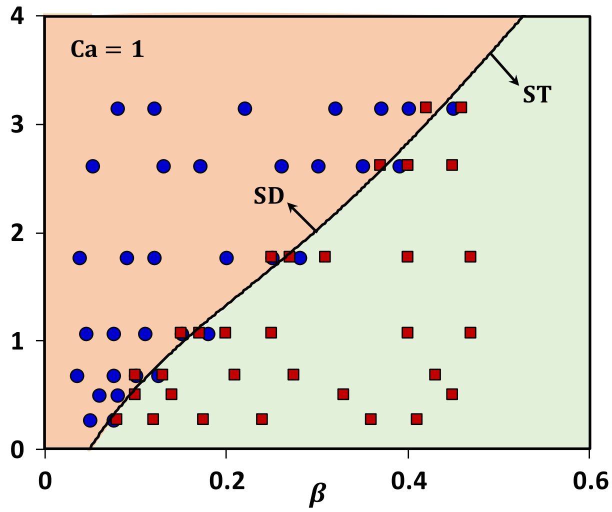

FIG. 4. The line representing the transition between the absolute and convective instability, i.e., $\tilde{v}^*_-(\mathrm{Ca},\beta,\xi) = 0$ for different values of β and ξ and fixed $\mathrm{Ca} = 1$, which demarcates the stream drop (SD) and stream thread (ST) regimes.

$\mathrm{Ca}_{\mathrm{ac}} > 1$. The droplets migrate to the channel center mainly due to the ARF, since the noninertial lift force [20] is much smaller compared to the ARF (see S9 in Supplemental Material [23]) and the acoustic streaming effect is negligible (see S15 in Supplemental Material, which includes Refs. [20,35,36,62–66]). The droplets can be isolated into a separate outlet compared to the continuous stream by satisfying the condition $\tau_{\mathrm{ac}} \ll \tau_{\mathrm{ad}}$ and designing the outlet channels such that the streamline passing through the center of the channel runs into the droplet isolation outlet (see Fig. S6 in Supplemental Material [23]). The droplets can contain particles, as shown in Fig. S7, which opens up the possibility of applying the technique for particle handling in microfluidics-based assays. Further, we find that the time required to achieve stream drop and drop-stream transition, from the time instant the acoustic field is turned on and off, respectively, is only $\sim$10 ms, so we achieve fast fluid handling. In contrast, the time required to achieve the above transition by varying the Ca of the phases is >100 ms (see S16 in Supplemental Material [23]). A much slower response (by more than one order) observed in the latter case is attributed to the response time of the fluidics system due to its inherent fluid capacitance.

In summary, we studied a reversible transition between stream and droplet regimes in a coflow system by tuning its exposure to acoustic waves at a fixed Ca. Given acousto-capillary number, $\mathrm{Ca}_{\mathrm{ac}} > 1$: for $\mathrm{Ca} < 1$, perturbation due to the acoustic force grows leading to absolute instability and droplet formation, and for $\mathrm{Ca} > 1$, the instability is convected downstream preventing droplet formation, and stream relocation is observed. The technique offers means of tuning from stream to droplet mode on demand, which can find applications in microfluidics, emulsification, and encapsulation.

A. K. S. thanks the Department of Science & Technology (DST), Government of India for providing financial support in the form of the Swarnajayanti Fellowship Award via Grant No. DST/SJF/ETA-30/2017-18. The support of Centre for NEMS and Nanophotonics, IIT Madras for device fabrication, and National Centre for Combustion Research & Development, IIT Madras for fluid property measurements are acknowledged.

---

[*] These authors contributed equally to this work.

[†] Corresponding author.
ashis@iitm.ac.in

[1] J. Plateau, Acad. Sci. Bruxelles Mém. **23**, 5 (1849).
[2] L. Rayleigh, Proc. R. Soc. **29**, 71 (1879).
[3] W. van Hoeve, S. Gekle, J. H. Snoeijer, M. Versluis, M. P. Brenner, and D. Lohse, Phys. Fluids **22**, 122003 (2010).
[4] T. Cubaud and T. G. Mason, Phys. Fluids **20**, 053302 (2008).
[5] A. M. Leshanskya and L. M. Pismen, Phys. Fluids **21**, 023303 (2009).
[6] C. N. Baroud, F. Gallaire, and R. Dangla, Lab Chip **10**, 2032 (2010).
[7] A. S. Utada, A. Fernandez-Nieves, H. A. Stone, and D. A. Weitz, Phys. Rev. Lett. **99**, 094502 (2007).
[8] C. Clanet and J. C. Lasheras, J. Fluid Mech. **383**, 307 (1999).
[9] B. Ambravaneswaran, H. J. Subramani, S. D. Phillips, and O. A. Basaran, Phys. Rev. Lett. **93**, 034501 (2004).
[10] A. S. Utada, A. Fernandez-Nieves, J. M. Gordillo, and D. A. Weitz, Phys. Rev. Lett. **100**, 014502 (2008).
[11] J. M. Gordillo, A. M. Gañán-Calvo, and M. Pérez-Saborid, Phys. Fluids **13**, 3839 (2001).
[12] A. Sevilla, J. M. Gordillo, and C. Martínez-Bazán, Phys. Fluids **17**, 018105 (2005).
[13] S. Tan, F. Maes, B. Semin, J. Vrignon, and J. C. Baret, Sci. Rep. **4**, 4787 (2014).
[14] M. L. Cordero1, F. Gallaire, and C. N. Baroud, Phys. Fluids **23**, 094111 (2011).
[15] S. D. Geschiere, I. Ziemecka, V. van Steijn, G. J. M. Koper, J. H. van Esch, and M. T. Kreutzer, Biomicrofluidics **6**, 022007 (2012).
[16] E. Hemachandran, S. Karthick, T. Laurell, and A. K. Sen, Europhys. Lett. **125**, 54002 (2019).
[17] J. T. Karlsen, P. Augustsson, and H. Bruus, Phys. Rev. Lett. **117**, 114504 (2016).
[18] M. Shojaeian, F. X. Lehr, H. U. Göringer, and S. Hardt, Anal. Chem. **91**, 3484 (2019).
[19] S. H. Tan, B. Semin, and J. C. Baret, Lab Chip **14**, 1099 (2014),
[20] E. Hemachandran, T. Laurell, and A. K. Sen, Phys. Rev. Applied **12**, 044008 (2019).
[21] R. Gaikwad and A. K. Sen, Analyst **146**, 95 (2021).
[22] H. Bruus, Lab Chip **12**, 1014 (2012).
[23] See Supplemental Material at http://link.aps.org/supplemental/10.1103/PhysRevLett.127.134501 for experimental setup, flow characterization, particle encapsulation and droplet isolation, numerical model and simulation results for acoustic streaming effect and stream breakup.
[24] A. A. Doinikov, M. S. Gerlt, and J. Dual, Phys. Rev. Lett. **124**, 154501 (2020).
[25] A. A. Doinikov, M. S. Gerlt, A. Pavlic, and J. Dual, Microfluid Nanofluid **24**, 32 (2020).
[26] L. Mazutis, J. Gilbert, W. L. Ung, D. A. Weitz, A. D. Griffiths, and J. A. Heyman, Nat. Protoc. **8**, 870 (2013).
[27] F. A. A. Fergusson, E. W. Guptill, and A. D. MacDonald, J. Acoust. Soc. Am. **26**, 67 (1954).
[28] J. Nebeker and T. R. Nelson, J. Ultrasound Med. **31**, 1389 (2012).
[29] B. Hartmann and J. Jarzynski, J. Acoust. Soc. Am. **56**, 1469 (1974).
[30] P. Somasundaran, S. C. Mehta, and P. Purohit, Adv. Colloid Interface Sci. **128–130**, 103 (2006).
[31] D. R. Karsa, *Design and Selection of Performance Surfactants* (CRC Press, Boca Raton, 1999), Vol. 2.
[32] A. Fornell *et al.*, Sci. Rep. **11**, 17501 (2021).
[33] J. T. Karlsen, W. Qiu, P. Augustsson, and H. Bruus, Phys. Rev. Lett. **120**, 054501 (2018).
[34] W. Qiu, J. T. Karlsen, H. Bruus, and P. Augustsson, Phys. Rev. Applied **11**, 024018 (2019).
[35] P. B. Muller, R. Barnkob, M. J. H. Jensen, and H. Bruus, Lab Chip **12**, 4617 (2012).

[36] H. Bruus, Lab Chip **12**, 1578 (2012).

[37] T. Pollak, A. Haas, and N. Aksel, Phys. Fluids **23**, 094110 (2011).

[38] M. J. Hancock and J. W. M. Bush, J. Fluid Mech. **466**, 285 (2002).

[39] G. Hertz and H. Mende, Z. Phys. **114**, 354 (1939).

[40] N. Bertin, H. Chraıbi, R. Wunenburger, J.-P. Delville, and E. Brasselet, Phys. Rev. Lett. **109**, 244304 (2012).

[41] B. Issenmann, A. Nicolas, R. Wunenburger, S. Manneville, and J.-P. Delville, Europhys. Lett. **83**, 34002 (2008).

[42] C. P. Lee and T. G. Wang, J. Acoust. Soc. Am. **94**, 1099 (1993).

[43] J. T. Karlsen, W. Qiu, P. Augustsson, and H. Bruus, Phys. Rev. Lett. **120**, 054501 (2018).

[44] P. Hahn, I. Leibacher, T. Baasch, A. Lamprecht, and J. Dual, Lab Chip **15**, 4302 (2015).

[45] COMSOL Multiphysics®. 5.4, http://www.comsol.com, 2018.

[46] P. Hahn and J. Dual, Phys. Fluids **27**, 062005 (2015).

[47] H. Bruus, Lab Chip **11**, 3742 (2011).

[48] J. Lei, M. Hill, and P. Glynne-Jones, Lab Chip **14**, 532 (2014).

[49] W. L. Nyborg, J. Acoust. Soc. Am. **30**, 329 (1958).

[50] P. Hahn, O. Schwab, and J. Dual, Lab Chip **14**, 3937 (2014).

[51] H. Bruus, Lab Chip **12**, 20 (2012).

[52] Z. Lu, E. D. Dupius, V. K. Patel, A. M. Momen, and S. Shahab, Phys. Fluids **33**, 032003 (2021).

[53] P. Yue, C. Zhou, J. J. Feng, C. F. Ollivier-Gooch, and H. H. Hu, J. Comput. Phys. **219**, 47 (2006).

[54] F. Gallaire and P. T. Brun, Phil. Trans. R. Soc. A **375**, 20160155 (2017).

[55] T. S. Kaminski, O. Scheler, and P. Garstecki, Lab Chip **16**, 2168 (2016).

[56] S. Chandrasekhar, *Hydrodynamic and Hydromagnetic Stability* (Oxford University Press, Oxford, 1968).

[57] C. A. Andersen, L. Alfine, K. Ohla, and R. Höchenberger, Behav. Res. Meth. Instrum. Comput. **51**, 2733 (2019).

[58] Y. J. Kang, E. Yeom, E. Seo, and S. J. Lee, Biomicrofluidics **8**, 014102 (2014).

[59] A. Nath and A. K. Sen, Phys. Rev. Applied **12**, 054009 (2019).

[60] T. R. Powers and R. E. Goldstein, Phys. Rev. Lett. **78**, 2555 (1997).

[61] P. Guillot, A. Colin, A. S. Utada, and A. Ajdari, Phys. Rev. Lett. **99**, 104502 (2007).

[62] S. Deshmukh, Z. Brzozka, T. Laurell, and P. Augustsson, Lab Chip **14**, 3394 (2014).

[63] L. P. Gor'kov, Phys. Doklady **6**, 773 (1962).

[64] K. Yosioka and Y. Kawasima, Acta Acust. Acust. **5**, 167 (1955).

[65] S. Z. Hoque and A. K. Sen, Phys. Fluids **32**, 072004 (2020).

[66] T. Baasch and J. Dual, J. Acoust. Soc. Am. **143**, 509 (2018).